Laterally-resolved formation mechanism of a lithium-based conversion layer at the matrix and intermetallic particles in aerospace aluminium alloys

Kosari, A.; Tichelaar, F.; Visser, P.; Zandbergen, H.; Terryn, H.; Mol, J. M.C.

DOI
10.1016/j.corsci.2021.109651

Publication date
2021

Document Version
Final published version

Published in
Corrosion Science

Corrosion Science 190 (2021) 109651

Contents lists available at ScienceDirect

Corrosion Science

journal homepage: www.elsevier.com/locate/corsci

Laterally-resolved formation mechanism of a lithium-based conversion layer at the matrix and intermetallic particles in aerospace aluminium alloys

A. Kosari [a,*], F. Tichelaar [b], P. Visser [c], H. Zandbergen [b], H. Terryn [d], J.M.C. Mol [a]

[a] Department of Materials Science and Engineering, Delft University of Technology, Mekelweg 2, 2628 CD, Delft, the Netherlands
[b] Kavli Institute of Nanoscience, Delft University of Technology, Lorentzweg 1, 2628 CJ, Delft, the Netherlands
[c] AkzoNobel, Rijksstraatweg 31, 2171 AJ, Sassenheim, the Netherlands
[d] Department of Materials and Chemistry, Research Group Electrochemical and Surface Engineering (SURF), Vrije Universiteit Brussel, Pleinlaan 2, 1050, Brussels, Belgium

ARTICLE INFO

Keywords:
AA2024-T3
Intermetallic particles
Dealloying
Lithium carbonate
Conversion coating
Passivation
TEM
FIB/SEM

ABSTRACT

Lithium leaching coatings have recently been developed as eco-friendly active corrosion protection technology for aerospace aluminium alloys (AAs) by the formation of a conversion layer at coating defects. While general conversion layer formation characteristics were studied and reported before, here we study the local layer formation process with sub-micron resolution at and around intermetallic particles (IMPs) in AA2024-T3. Top- and cross-sectional-view morphological electron micrograph observations along with open circuit potential (OCP) measurements are performed, mimicking coating defect conditions upon lithium carbonate leaching from the coating matrix. The results revealed five stages of the conversion process in which the alloy matrix and different IMPs evolve morphologically, compositionally, and electrochemically. Besides, we found a correlation between the OCP response of the AA2024-T3 system and the morphological and compositional evolutions of the alloy matrix and IMPs at different stages of exposure. Passive layer and alloy matrix dissolution leading to surface Cu-enrichment and S-phase dealloying occur at early stages of exposure. They precede the formation of a columnar layer on the alloy, followed by the establishment of a dense-like layer at the final stage. Dealloying of Al_2CuMg can assist the conversion process by providing local supersaturation. Through complementary experiments in a sodium carbonate solution and besides X-ray diffraction analysis, we found out that lithium plays a critical role in stabilising the corrosion product throughout the conversion process.

1. Introduction

In recent years, lithium salts have drawn high attention as hexavalent chromium-free corrosion inhibitors due to a passivating character for a variety of aluminium alloys (AAs) [1–5]. However, the preliminary investigations go back to 1987 when Gui and Devine observed an unexpected passivity while anodically polarising AA6061-T6 in an alkaline lithium carbonate solution [6]. In 1994, Buchheit et al. generated protective hydrotalcite conversion coatings by immersing AAs in an alkaline lithium carbonate solution followed by heat treatment at a relatively low temperature in air [7]. Later, Drewien et al. confirmed the formation of Li-Al layered double hydroxide (Li-Al LDH) on AA1100 through a conversion layer process in a lithium carbonate-lithium hydroxide solution (pH 11–12) [8]. Another major breakthrough was established many years later in 2010 when Visser and Hayes showed that lithium salts can be incorporated into organic coatings to provide active corrosion protection [9]. In this scheme, incorporated lithium salts [10,11] are released with a long-range throwing power at damaged coating locations [12], establishing an alkaline environment of approximately pH 10 [13]. In the presence of lithium, this is associated with the formation of an irreversible conversion layer at the coating defect that can effectively and reliably protect the AA substrate [14]. Thereafter, the studies were dedicated to characterising the generated layer in artificial scribes subjected to neutral salt spray (NSS) exposure [15,16].

Up to now, detailed structural and compositional studies have revealed a uniform distribution of lithium throughout the conversion layer which appears in a multi-layered arrangement depending on the

* Corresponding author.
E-mail address: a.kosari@tudelft.nl (A. Kosari).

https://doi.org/10.1016/j.corsci.2021.109651
Received 30 April 2021; Received in revised form 16 June 2021; Accepted 22 June 2021
Available online 24 June 2021

location in the scribe [17]. In general, there is a columnar outer layer identified as Li-Al LDH and a dense inner layer which represents an amorphous lithium-containing pseudoboehmite phase [17]. Besides, a porous layer in which both amorphous and crystalline compounds co-exist resides in between [17]. Extensive electrochemical evaluations have shown that the conversion layer can well protect AAs substrate; the inner dense layer shows the highest barrier properties compared to other two sublayers [18].

Regarding the formation mechanism, the studies have indicated that the lithium-based conversion layer goes through several morphological and compositional stages from initiation to completion. In one of their works, Visser et al. set up an electrochemical cell representing the aqueous conditions of a scribe area exposed to lithium carbonate-sodium chloride solution [19]. Combined with compositional and morphological investigations, they proposed three consecutive stages of oxide thinning, anodic dissolution and hydroxide film formation, and growth. In fact, the final stage occurs through a competitive film formation and dissolution process, leading to transformation of the outer aluminium hydroxide layer into a Li-Al LDH. However, the studies have so far been dedicated to exploring the mechanism and the different stages of the conversion layer formation on the alloy matrix more than at and around intermetallic particles (IMPs).

Intermetallic phases in aerospace AAs significantly contribute to their mechanical properties, but they bring along a deteriorated corrosion resistance due to their higher electrochemical activity compared to the alloy matrix [20–24]. Therefore, local corrosion evidently takes place at IMPs locations [25–28]. Given the local, heterogeneous and enhanced electrochemical activity induced by IMPs in AAs, it is therefore particularly crucial in corrosion inhibition strategies to consider and optimise the protection at and around IMPs. So, the current work focused on gaining detailed understanding of the conversion layer formation at and around different types of intermetallic compounds in AA2024-T3. We endeavour to find a correlation between the substrate's overall electrochemical response and the local morphological evolutions at different stages of exposure. To this end, we record the open circuit potential (OCP) of AA2024-T3 exposed to a lithium carbonate–sodium chloride solution for 7 h. In parallel, top-view and cross-sectional morphological observations are conducted by means of focused ion beam/scanning electron microscopy (FIB/SEM) analysis to provide further insights into different stages of the conversion layer formation related to intermetallic phases in particular. Moreover, X-ray diffraction (XRD) analysis are performed to confirm the role of lithium in the conversion process.

2. Materials and methods

AA2024-T3 sheets were SiC ground to #1200 and then polished on a soft cloth in alumina slurries of 0.5 and 0.05 μm in a non-aqueous solution. The samples were placed in an electrochemical cell setup providing an exposed area of 3.14 cm^2. The cell was filled with 1.23 mL of 0.01 M NaCl + 0.01 M Li_2CO_3 solution (pH 10.6), providing a relatively thin-film electrolyte condition (approx. 4-mm thick) representative for the scribe area. According to Visser et al. [13,19], such a solution composition is fairly representative for lithium concentration and pH in a defect area of 1 mm wide upon lithium carbonate leaching from the coating. In this estimation, different parameters including the coating thickness [10], lithium carbonate loading [9], volume of defect area and the lithium depletion depth [12] in the coating were considered. The open circuit potential (OCP) of the samples exposed to the aerated solution were recorded versus an Ag/AgCl saturated reference electrode for the duration of 7 h. Prior investigations have shown that the conversion process can proceed to an advanced stage of formation within this period of exposure [19]. From the typical OCP evolution behaviour, different exposure times were chosen at which subsequent exposure tests were stopped for detailed microscopic investigations of the conversion layer formed at those times. In addition, we have exposed AA2024-T3 samples to a lithium-free 0.01 M NaCl + 0.01 M Na_2CO_3 solution (pH 10.6) and in an identical condition in terms of the electrolyte thickness (approx. 4 mm) in order to understand lithium impact on the layer formation and OCP evolutions.

Prior to preparation for microscopic analysis, samples were rinsed with flowing distilled water in order to quench the conversion layer formation process. FIB/SEM cross-sectioning was carried out over different areas of the exposed samples by means of a Thermo-Fisher Helios G4 FIB/SEM microscope. The top-view and cross-sectional SEM morphological studies were performed at 15 keV collecting emitted secondary electrons (SE) in ultra-high-resolution mode. The chemical composition of individual IMPs was estimated using energy dispersive spectroscopy (EDS - not shown here). FIB sectioning was conducted in a blind-mode, whereby the ion beam was used only for milling. It allows us to omit providing a Pt or C overlay process for protection of the top surface from Ga ion-beam damage. Besides, the thin TEM cross-sections were fabricated out of regions of interest with FIB and lift-out procedure [29] for detailed structural and composition investigations. Elemental analysis of the specimens was carried out with the Thermo-Fisher Super-X Detection System installed on a Cs corrected Thermo-Fisher Titan 300 kV TEM.

X-Ray diffraction (XRD) measurements were carried out with a Bruker D8 Discover diffractometer and Eiger-2 500k 2D-detector. The samples exposed to 0.01 M NaCl + 0.01 M Li_2CO_3 for 2 and 7 h were radiated by Cu-Kα X-ray continuously from 10° to 25° (2θ) at a step size of 0.040°/2θ and a counting time of 1 s per step. Then, the acquired data were analysed by means of Bruker software DiffracSuite.EVA vs 5.2.

3. Results and discussion

3.1. OCP evolution during the conversion layer formation

Fig. 1 shows the representative OCP behaviour of the AA2024-T3 sample exposed to 0.01 M NaCl + 0.01 M Li_2CO_3 over time. According to the OCP evolution, we can identify five distinct stages of the conversion layer formation. Stage I shows up as a sharp initial drop from −1150 mV to a minimum of −1420 mV during the first 60 s. Immediately after, the system experiences the first increase in the OCP values, reaching a plateau of −1220 mV at 800 s. Stage III appears as the second rise in the OCP towards a plateau of −1000 mV after more than 1 h. The stage IV is associated with the third rise in the OCP values gradually reaching −600 mV at 4 h. From this point onwards, the system reveals a

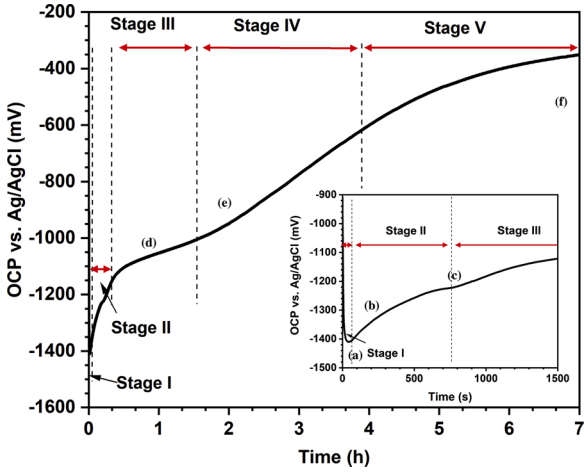

Fig. 1. Open circuit potential (OCP) evolution of AA2024-T3 exposed to 0.01 M NaCl + 0.01 M Li_2CO_3 (pH 10.6). Five stages can be considered for the conversion layer formation. Based on that, we have picked exposure times of (a) 60 s, (b) 200 s, (c) 800 s, (d) 2800s, (e) 2 h and (f) 7 h to study the morphological evolutions of the conversion layer with time.

nearly stabilised behaviour (Stage V) where the OCP slightly changes to −400 mV after a total exposure of 7 h.

It should be noted that OCP represents an electrochemical situation in which the total anodic and cathodic currents are equal. Thus, any modification related to anodic/cathodic reactivities as a consequence of the gradual morphological and compositional evolutions on the surface can cause an impact on the electrochemical response of the system, here OCP values [30]. Therefore, we study the different phases including the alloy matrix and intermetallic compounds to see how they individually contribute to the OCP values during the conversion process. Given the OCP evolution with time, the samples were therefore taken at the certain exposure times of the formation. The time intervals include 60 s (Late Stage I), 200 s (Early Stage I), (late Stage I) 800 s, (Stage III) 2800s, 2 h (Stage IV) and 7 h (Stage V), representing distinct times of exposure emerging in the OCP graph. It should be stated that the OCP profiles of AA2024-T3 in 0.01 M NaCl + 0.01 M Li_2CO_3 generally show an identical trend. However, owing to intrinsically heterogeneous microstructure of AA2024-T3, the OCP values of different samples show dissimilarities in particular at moderate stages, although no significant differences are observed at early and late stages of exposure (See Fig. S1 in Supplementary Material). Thus, the exposure periods are picked at times at which OCP values reveal highest similarities since AA2024-T3 samples are exposed separately for morphological investigations.

3.2. *Morphological characterisation of the conversion layer on the alloy matrix at different exposure times*

Fig. 2 shows top-view SEM images of the AA2024-T3 surface after the specific periods of exposure to 0.01 M NaCl + 0.01 M Li_2CO_3 solution. Fig. 3a reveals that the polished surface has been slightly corroded during the first 60 s of the exposure. At 200 s (Fig. 2b), we observe a roughened morphology for the surface, indicating further corrosion of the alloy matrix. After 800 s (Fig. 2c), we see that the surface has started to turn into a different top-view configuration, acquiring a petal-like morphology. Prolonged exposure until 2800 results in the appearance of a clear layer on the alloy surface (Fig. 2d). Fig. 2e shows a more pronounced petal-like morphology after 2 h (Fig. 2e). This is a clear indication of the conversion layer formation over the alloy matrix, in particular after 7 h when the petals have considerably grown (Fig. 2f).

Fig. 3 shows the SEM images of the FIB cross-sections when the stage is at 52° tilt. As is evident in Fig. 3a and b, the initial exposure to 0.01 M NaCl + 0.01 M Li_2CO_3 until 200 s does not lead to the conversion layer formation. This implies that the alloy matrix merely undergoes dissolution at this stage. After 800 s, we observe the formation of a very thin (hydr)oxide layer (approx. 50 nm) on the alloy surface (Fig. 3c). The cross-sectional SEM image at 2800s (Fig. 3d) indicates the formation of a conversion layer in a columnar morphology, preceding other reported sublayers. Prolonged exposure until 2 h is associated mainly with the columnar layer thickening, although a dense-like layer has appeared at some locations, indicated by the blue arrow (Fig. 3e), owing to different local activities and thus local solution chemistry. However, a 7-h exposure comes along with the confirmation of a uniform dense-like layer formation close to the alloy substrate as clearly shown in Fig. 3f. Besides, the columnar layer has slightly grown as compared to the layer grown for 2 h. In general, the top-view and cross-sectional SEM images confirm different formation stages of the conversion layer gradually covering the entire alloy matrix. It should be stressed that here we report on the morphological evolutions at different stages while the sublayers can endure compositional and structural modifications during the conversion process also [15].

Characterised in the several studies, the conversion layer is mainly composed of aluminium, lithium and oxygen [15,17,19]. The studied solution holds lithium, however aluminium needs to be supplied through the direct anodic dissolution of the alloy matrix. Thus, the cathodic reactions (i.e., dominantly water reduction) come about in return for charge neutralisation. This phenomenon is associated with the local nucleation and growth of hydrogen bubbles at some locations (i.e., IMPs), leading to the gradual de-wetting of the regions involved. Regions that get de-wetted at later stages of exposure reveal different surface morphologies as compared to those de-wetted earlier. Since every single morphology is related to a distinct stage of the conversion process, the morphological variations owing to such a local phenomenon can be considered instructive to better understand the mechanisms behind the conversion layer formation. In this regard, Fig. 4a shows the SEM images of a hydrogen bubble footprint; the sample was exposed for 7 h. The inset is the optical macrograph of the alloy surface being exposed to the solution after about 7 h. As can be seen, the gradual de-wetting has resulted in a different surface morphology, representing different stages of the conversion process. A closer look at the green rectangular region is shown in Fig. 4b. According to the top-view

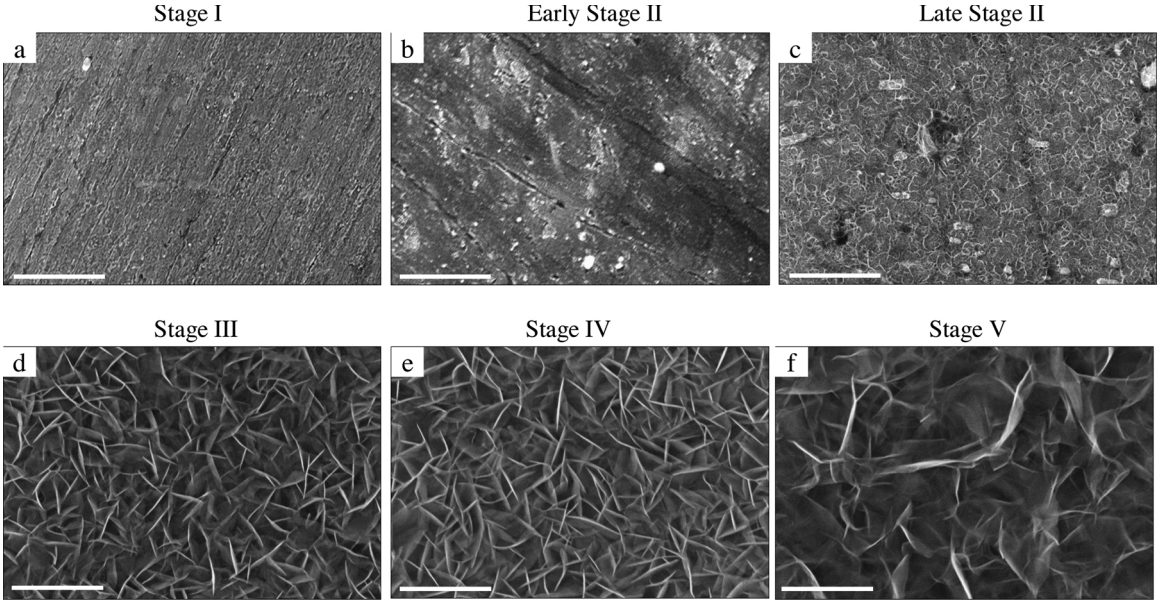

Fig. 2. Top-view observations of the conversion layer exposed to 0.01 M NaCl + 0.01 M Li_2CO_3. SEM images of AA2024-T3 surface at different exposure times of (a) 60 s; (b) 200 s; (c) 800 s; (d) 2800s; (e) 2 h; (f) 7 h. The scale bar represents 1 μm.

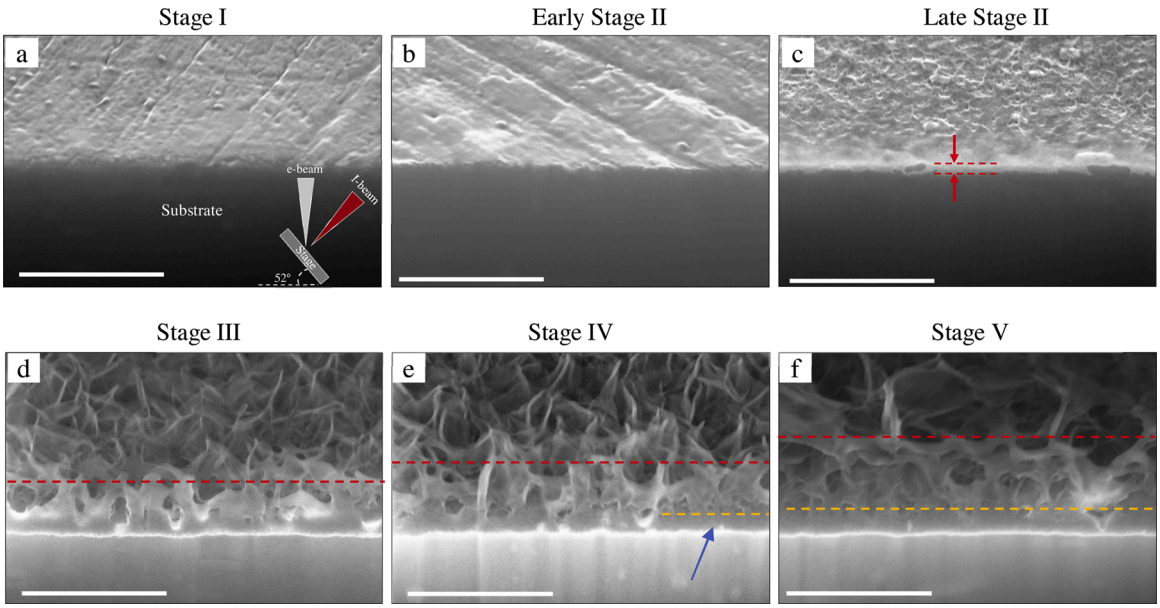

Fig. 3. Cross-sectional observations of the conversion layer exposed to 0.01 M NaCl + 0.01 M Li_2CO_3. SEM images of AA2024-T3 surface at different exposure times of (a) 60 s; (b) 200 s; (c) 800 s; (d) 2800s; (e) 2 h; (f) 7 h. The sections are made using FIB milling. The red dashed lines indicate the highest location in the conversion layer at each stage. The orange dashed line separates the columnar layer from the dense-like layer. The blue arrow in Fig. 3e points at the location at which a dense-like layer is observed. The scale bar is 1 μm.

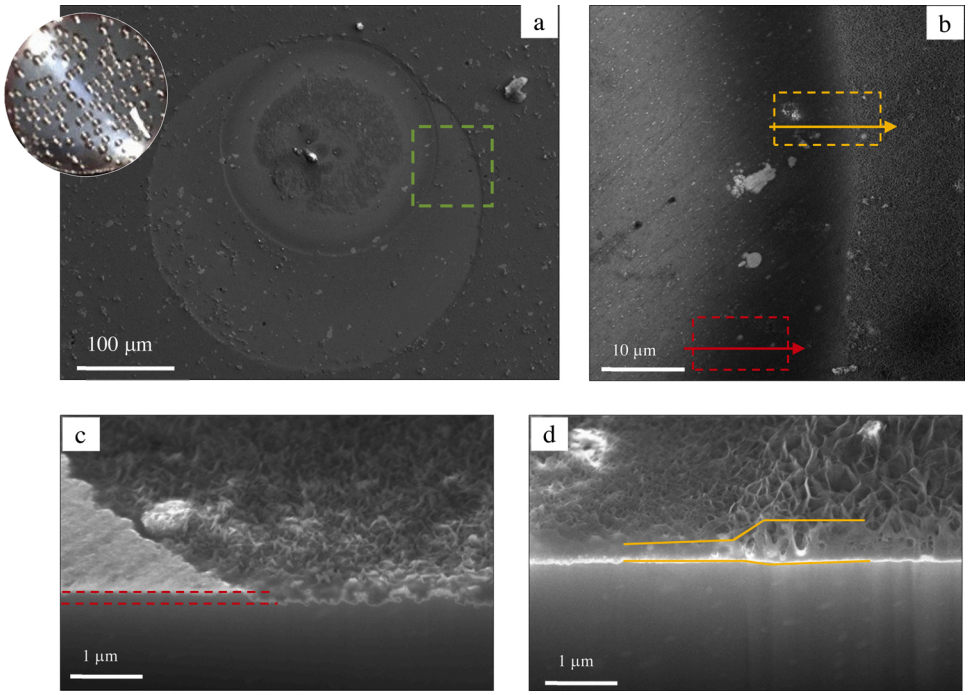

Fig. 4. Top-view and cross-sectional observation of the conversion layer at the bubble locations. (a) Top-view SEM image of the surface morphology around a bubble formed as a consequence of hydrogen evolution reactions. The bubbles initiate at several locations on the surface and grow with time. Thus, different stages of the layer formation can be recognised within the bubble regions. The inset shows the bubbles formed on AA2024-T3 surface after 7 h of exposure. (b) Top-view SEM image of the green rectangular regular region shown in Fig. 4a. (c) Cross-sectional SEM image of the region along the red dashed rectangle shown in Fig. 4b. (d) Cross-sectional SEM image of the region along the yellow arrow (yellow dashed rectangle) shown in Fig. 4b. The sections are made via FIB milling.

morphology, the red arrow approximately denotes the transition from Stage I to Stage III. Furthermore, the yellow arrow includes Stage III to Stage V. Fig. 4c shows the cross-sectional SEM image corresponding to the red rectangular region. As is evident, the alloy matrix has endured dissolution before appearance of the primary conversion precipitate. As reported by Drewien et al. [8], the supersaturation by $Al(OH)_4^-$ of the solution is critical for formation of the conversion layer. In fact, the alkaline solution continues to dissolve the alloy surface until reaching the required supersaturation at the surface. Fig. 4d shows the SEM image of the cross-section corresponding to the yellow rectangular region. Going over the image from left to right, we observe that the dissolution front slightly penetrates into further depth while the columnar layer/-solution interface increases to a higher level, implying a dissolution/precipitation process at the advanced stages of the conversion layer formation.

3.3. *Morphological characterisation of the conversion layer on IMPs at different exposure times*

Fig. 5 shows morphological observations of different intermetallic phases in AA2024-T3 exposed to 0.01 M NaCl + 0.01 M Li_2CO_3 for 60 s. At this stage, we see no indication of the layer formation over all the

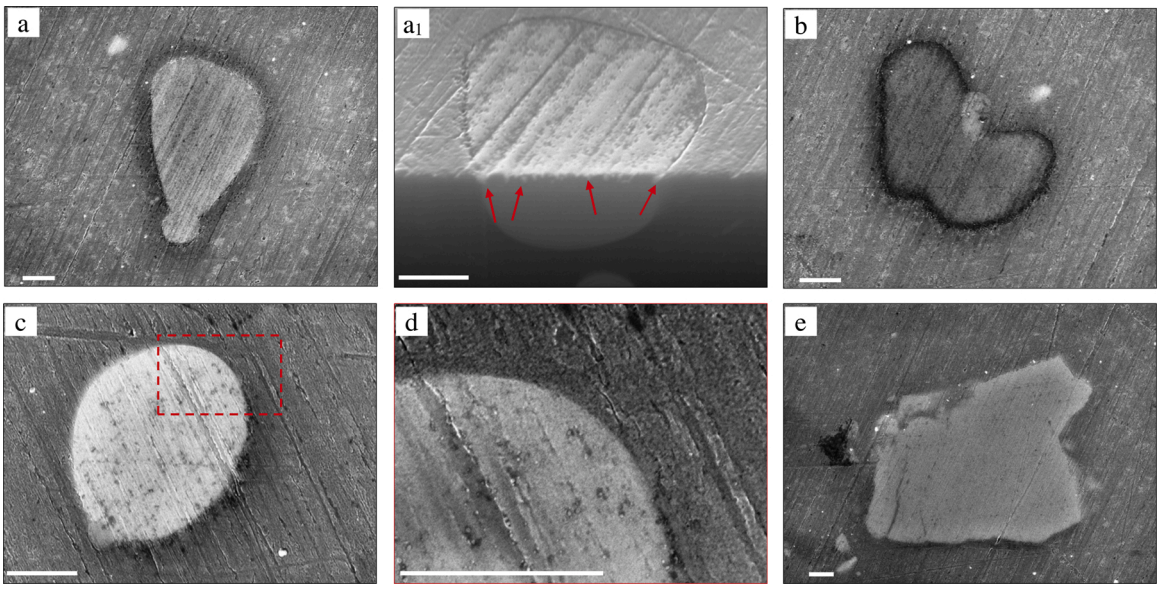

Fig. 5. Morphological observations of intermetallic phases in AA2024-T3 exposed to 0.01 M NaCl + 0.01 M Li_2CO_3 for 60 s. (a and a_1) Top-view and cross-sectional SEM images of an Al_2CuMg particle. The red arrows indicate the slightly-dealloyed regions in the particle. (b) Top-view SEM image of an Al_2CuMg particle; the peripheral shallow trench around the particle looks darker in contrast. (c) Top-view SEM image of an Al_2Cu particle. (d) The magnified view of the rectangular region indicated in Fig. 5c. (e) Top-view SEM image of a constituent-phase particle. The scale bar is 1 μm.

IMPs and they look still bare. Fig. 5a and a_1 shows top-view and cross-sectional SEM mages of an S-phase particle. The top-view image shows a dark ribbon all around this particle. The FIB cross-section reveals that this peripheral region has slightly been trenched at this stage. Besides, we see that the corrosion has penetrated into the particle at some locations as shown by the red arrows. We later confirm that selective dissolution of aluminium and magnesium from S-phase (i.e., dealloying) gradually occurs in the studied solution. Fig. 5b shows another S-phase particle showing a similar corrosion-attack morphology. Furthermore, Al_2Cu and constituent phase particles are found almost intact at this stage; see Fig. 5c–e. It should be mentioned that constituent phases are Al, Fe, Si, Mn and Cu-containing particles which are formed during the alloy solidification [31].

Fig. 6 shows the top-view and cross-sectional morphology of different IMPs after 200 s. It is obvious that the S-phase particles have undergone a clear change in morphology. Fig. 6a-a_2 reveal formation of a petal-like layer on the S-phase particle while the surrounding alloy matrix is still bare. The cross-sectional SEM image indicates further penetration of the dealloying and the alloy trenching into depth. It seems that a fast release of $Al(OH)_4^-$ ions from the Al_2CuMg particle due to dealloying provides the local supersaturation for the conversion process. This actually happens via a two-step electrochemical/chemical reaction of Al^{3+} to $Al(OH)_3$ and then to $Al(OH)_4^-$ under the alkaline conditions [32]. This has led to the formation of the petal-like layer

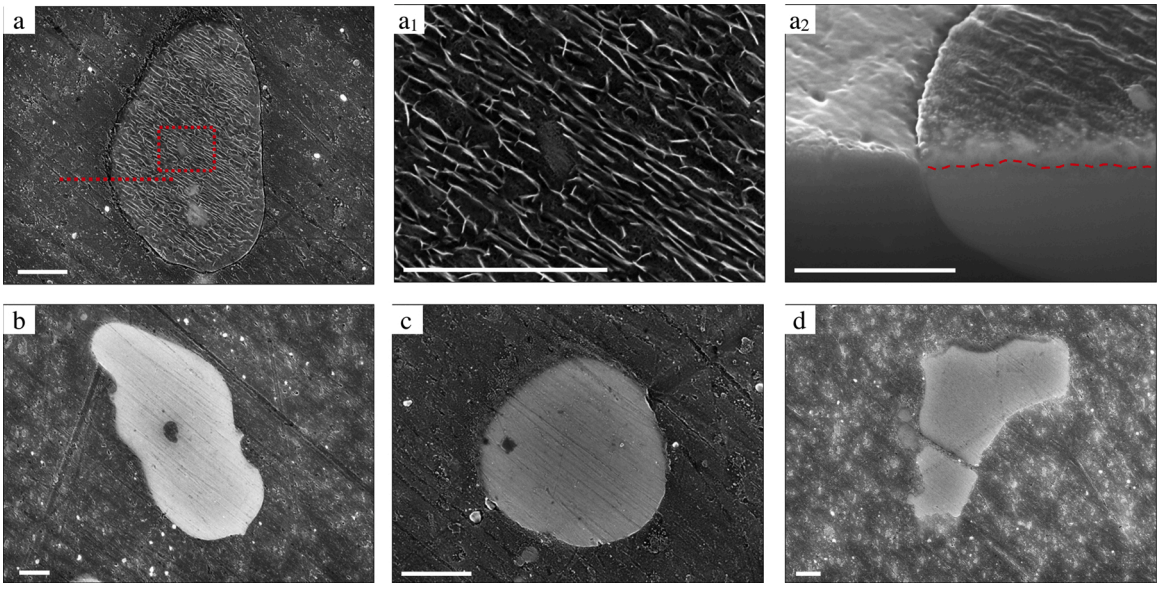

Fig. 6. Morphological observations of intermetallic phases in AA2024-T3 exposed to 0.01 M NaCl + 0.01 M Li_2CO_3 for 200 s. (a, a_1 and a_2) Top-view and cross-sectional SEM images of an Al_2CuMg particle. The top-view SEM image reveals the initial formation of a columnar layer on the particle. (a_1) shows the magnified view of the rectangular region indicated in Fig. 6a. (a_2) shows the cross-sectional SEM image along the red dashed line indicated in Fig. 6a, revealing the dealloyed top region in the particle. (b and c) Top-view SEM image of two Al_2Cu particles. (d) Top-view SEM image of a constituent-phase particle. The scale bar is 1 μm.

merely over the S-phase particles and not yet on the alloy matrix. In contrast, Al_2Cu and constituent phase particles have still not been involved in the conversion process (see Fig. 6b–d).

Fig. 7 shows top-view and cross-sectional micrographs of representative IMPs after 800 s. As can be seen in Fig. 7a and a_1, the conversion layer on the S-phase has insignificantly changed while the surrounding alloy matrix has acquired a similar morphology. The cross-sectional SEM image reveals that the dealloying has propagated more into depth at the peripheral regions of the particle where the alloy matrix has been trenched tightly around the particle. This behaviour has also been observed in uninhibited NaCl solutions [25]. Interestingly, Al_2Cu and constituent phase particles and their close vicinity are still uncovered; the bare regions are indicated by the red closed curves in Fig. 7b and c. This phenomenon is caused by the lack of $Al(OH)_4^-$ ions which are essential for the conversion layer process. In fact, these two phases are rather electrochemically stable and slightly endure dealloying, resulting in limited concentration of $Al(OH)_4^-$ ions which need to be supplied from the dissolution of the adjacent alloy matrix. This also explains why a solution locally dilute in $Al(OH)_4^-$ ions exists around Al_2Cu and constituent phase particles, causing a delay in the layer formation.

After 2800s, we found all the IMPs fully covered by the conversion layer revealing a petal-like top-view morphology (Fig. 8). As can be seen in top-view and cross-sectional SEM images (Fig. 8a and a_1), the S-phase particle has further but slightly been dealloyed, in particular, at the particle/alloy matrix interface (mind the corresponding inset). The formed layer has the character of a columnar morphology from a cross-sectional point of view [17]. The conversion layer formed on both Al_2Cu (Fig. 8b and b_1) and constituent phase particles (Fig. 8c and c_1) is similar to that on the S-phase from a top- and cross-sectional view. No significant indication of dealloying and trenching is observed in these two phases. However, the top surface of the Al_2Cu and constituent phase particles has been slightly dealloyed since they are more electrochemically stable than S-phase [25,26]. Besides their dealloying happens sluggishly in the studied solution. It means that the dissolution of their surrounding alloy matrix has provided the saturation of the local solution by $Al(OH)_4^-$ ions required for the layer formation. Given the OCP curve (Fig. 1), the system is actively evolving towards the positive values; this is a clear indication of passivity acquirement [32].

Prolonged exposure up to 2 h has resulted in the further growth of the conversion layer. All the IMPs have insignificantly changed in terms of morphology of the lithium-based layer (Fig. 9). However, it is remarkable that the layer over the IMPs is still thickening. Afterwards, the AA2024 sample starts to stabilise based on the OCP values, nearly reaching a plateau of −400 mV after 7 h. At this stage, the top-view petal-like morphology has considerably coarsened (Fig. 10). The S-phase particle has partly dealloyed, although there is a deep penetration of dealloying at the particle/matrix interface (Fig. 10a and a_1). A dense-like sublayer has appeared in the conversion layer formed on the alloy matrix at this stage; however, the columnar layer is still observed over the S-phase particle. This is also the case for the other types of IMPs (i.e., Al_2Cu and constituent phase particles). The fact is that the dense-like layer forms at the latest stage of the exposure due to further but slowed-down penetration of corrosion into alloy matrix. This phenomenon that cannot take place on the IMPs is associated with the formation of a layer with less porosities. The growth of the columnar layer on the IMPs is a consequence of the direct precipitation from the saturated solution which will be discussed later.

To explore how the dealloying can accelerate the formation of the conversion layer, we take a closer look at the S-phase particles with Scanning TEM/energy dispersive spectroscopy (STEM/EDS). The TEM cross-sections were prepared with FIB and lift-out procedure out of the S-particles exposed to the identical solution for 7 h. Fig. 11 shows an S-phase particle which has been dealloyed partly. It should be mentioned that the dealloying morphology of this particle is a bit different than that of other S-phase particles in this study as it has been exposed to a different amount of 0.01 M NaCl + 0.01 M Li_2CO_3 solution (electrolyte thickness of approx. 2 mm) for 7 h which shows an effect on the morphology of the dealloying and conversion layer. S-phase is known as an intermetallic compound with a high electrochemical instability in a wide range of solution pH, generally undergoing dealloying due to preferential dissolution of aluminium and magnesium and also rearrangement of copper in a nano-porous morphology [25]. The cross-sectional STEM image shows a nano-porous dealloying morphology in the periphery of the particle; the dealloying is penetrated more into the particle from the bottom part. Besides, it is remarkable that the conversion layer on the particle and on its adjacent matrix has the same thickness. However, the dense layer is missing on the particle and it merely composes of a columnar layer. Besides, corrosion products

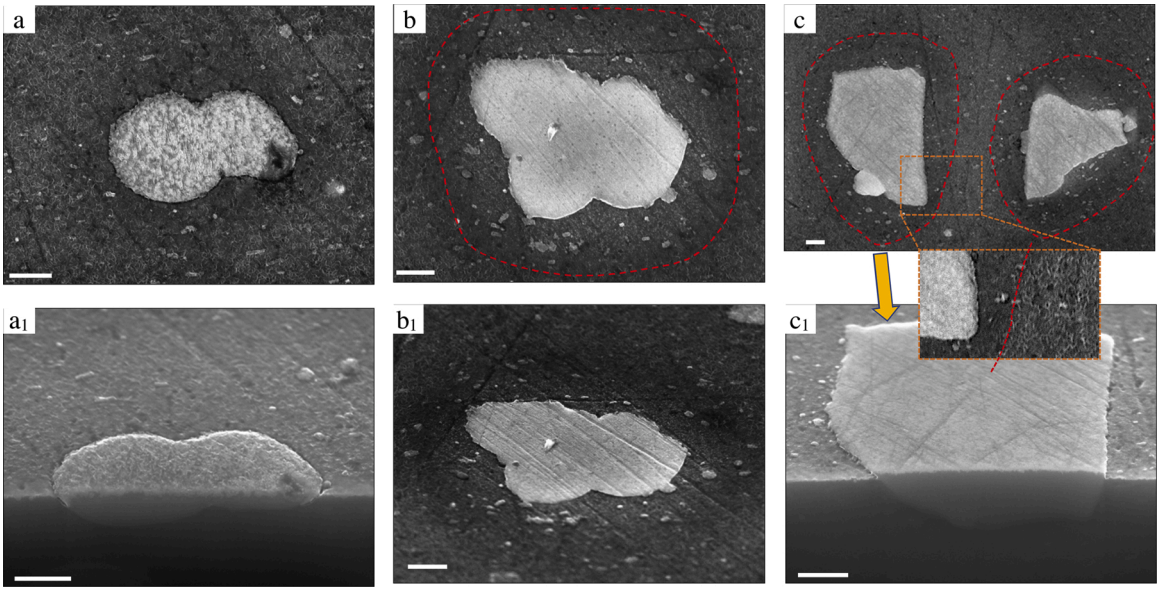

Fig. 7. Morphological observations of intermetallic phases in AA2024-T3 exposed to 0.01 M NaCl + 0.01 M Li_2CO_3 for 800 s. (a and a_1) Top-view and cross-sectional SEM images of an Al_2CuMg particle. A columnar layer has formed on the particle and also on the adjacent alloy matrix around it. (b and b_1) SEM images of an Al_2Cu particle; (b) stage tilt 0° and (b_1) stage tilt 52°. The columnar layer is merely observed outside the red closed curve. (c and c_1) Top-view and cross-sectional SEM image of a constituent-phase particle. As is evident in the inset, there is no columnar layer formed within the closed curves. The scale bar is 1 μm.

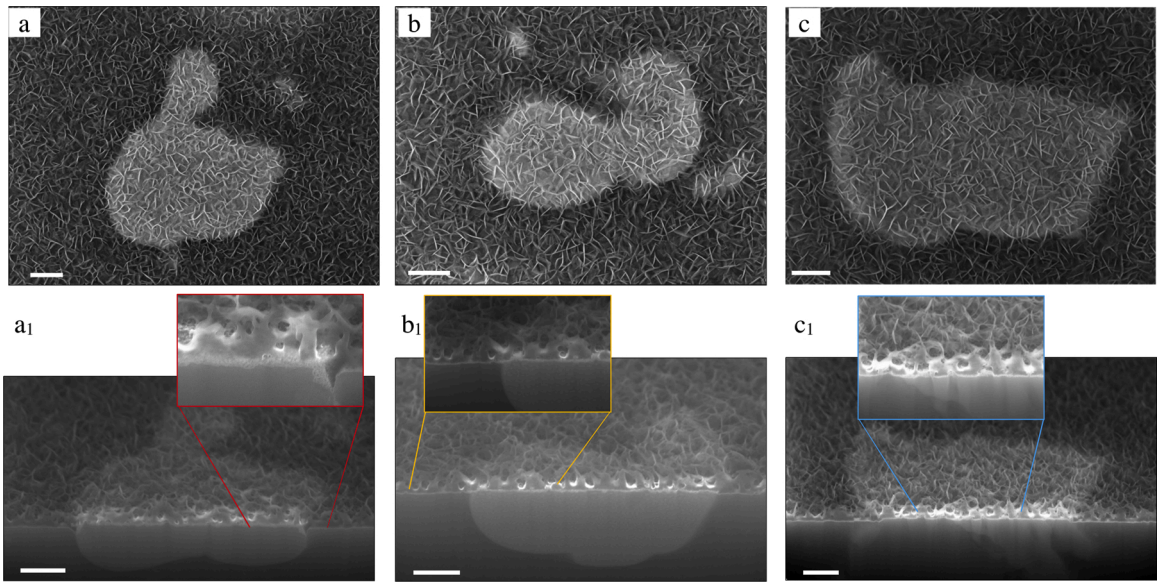

Fig. 8. Morphological observations of intermetallic phases in AA2024-T3 exposed to 0.01 M NaCl + 0.01 M Li_2CO_3 for 2800s. Top-view and cross-sectional SEM images of (a and a_1) an Al_2CuMg particle, (b and b_1) an Al_2Cu particle and (c and c_1) a constituent-phase particle. The insets are the magnified views of the indicated cross-sectional regions. At this stage, the top-view images reveal the entire alloy matrix and IMPs are covered with a columnar layer. The scale bar is 1 μm.

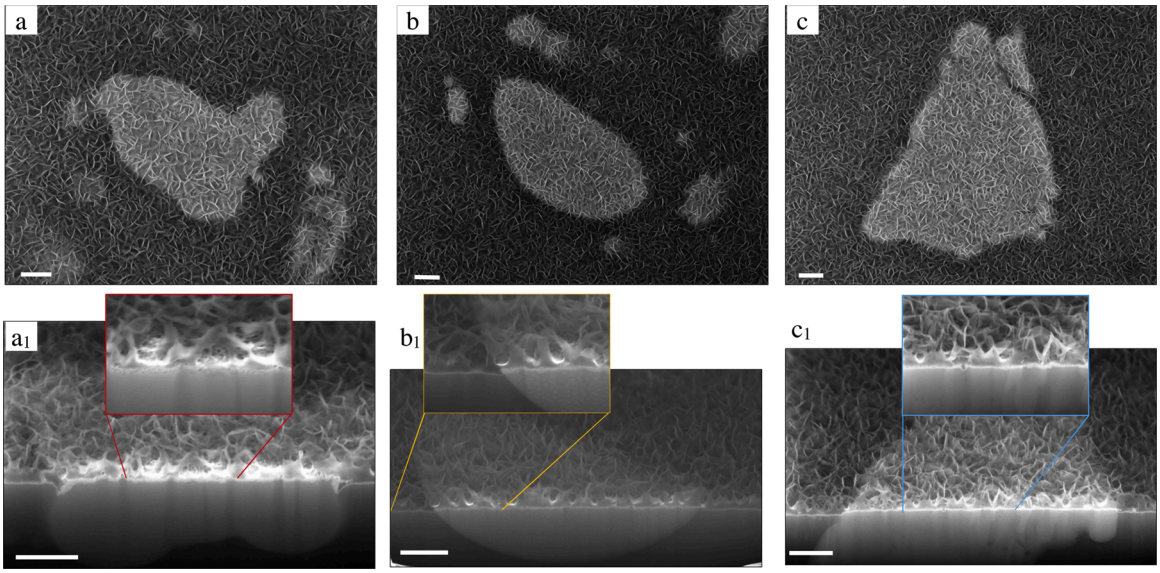

Fig. 9. Morphological observations of intermetallic phases in AA2024-T3 exposed to 0.01 M NaCl + 0.01 M Li_2CO_3 for 2 h. Top-view and cross-sectional SEM images of (a and a_1) an Al_2CuMg particle, (b and b_1) an Al_2Cu particle and (c and c_1) a constituent-phase particle. The insets are the magnified views of the indicated cross-sectional regions. The scale bar is 1 μm.

with a similar morphology to the dense layer is formed within the trench. The corresponding EDS elemental maps (Fig. 11) show that the dealloyed regions of the particle are depleted from magnesium. Given that magnesium is insoluble in solutions of pH higher than 12, herein its preferential dissolution is plausible as the studied solution provides insufficient alkalinity for the stability of magnesium. Aluminium dissolution has happened to a lesser extent; however, the formation of a dense-like layer within the trench implies the role of lithium intercalation in stabilisation of aluminium-based corrosion products. As expected, copper does not endure dissolution, as long as the corroding particle is connected to the matrix, and it has rearranged in a nano-porous morphology.

3.4. XRD analysis of the formed conversion layer

XRD patterns collected from the samples exposed for 2 and 7 h to are shown in Fig. 12. The presence of Li-Al LDH can be identified through the appearance of characteristic (003) and (006) peaks [8]. Since X-ray interactions takes place with an atom's electron cloud [33], the atomic scattering factors are relatively low for Li, C and Al which contribute to the intensity of basal reflections in Li-Al LDH. Thus, X-rays get scattered to a minor extent only while traveling through the thin surface conversion layers which leads to emerging reflections originating from the IMPs. This is particularly problematic for Li-Al LDH identification since the strong reflections corresponding to Al_7Cu_2Fe show up at the grazing angles very close to the characteristic Li-Al LDH peaks. This is evident in Fig. 12 where the (002) peaks of Al_7Cu_2Fe make the basal reflections

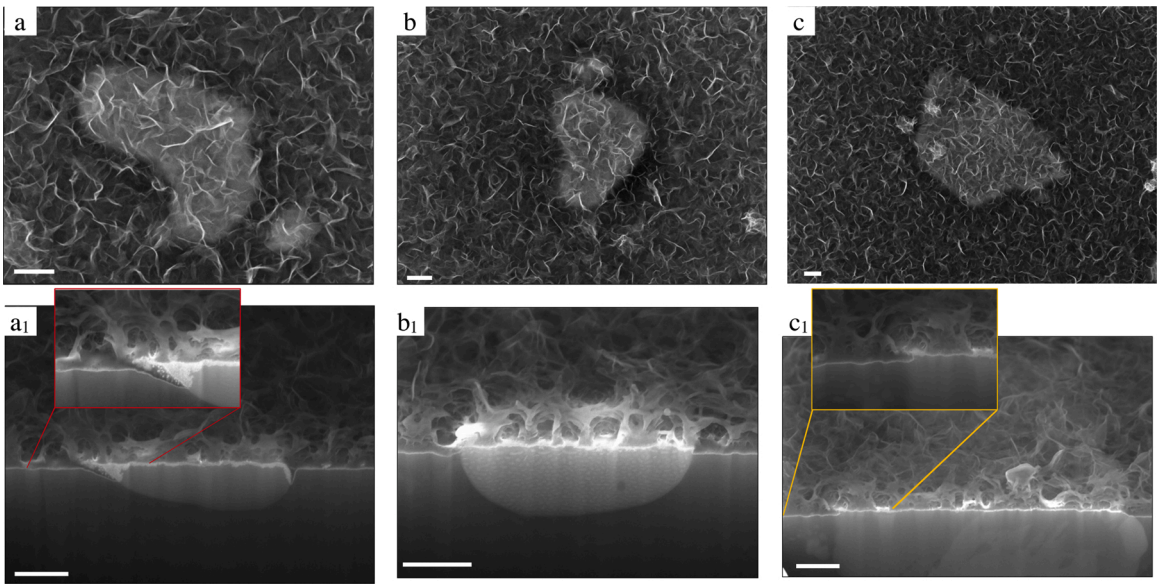

Fig. 10. Morphological observations of intermetallic phases in AA2024-T3 exposed to 0.01 M NaCl + 0.01 M Li_2CO_3 for 7 h. Top-view and cross-sectional SEM images of (a and a_1) an Al_2CuMg particle, (b and b_1) an Al_2Cu particle and (c and c_1) a constituent-phase particle. The insets are the magnified views of the indicated cross-sectional regions. The scale bar is 1 μm.

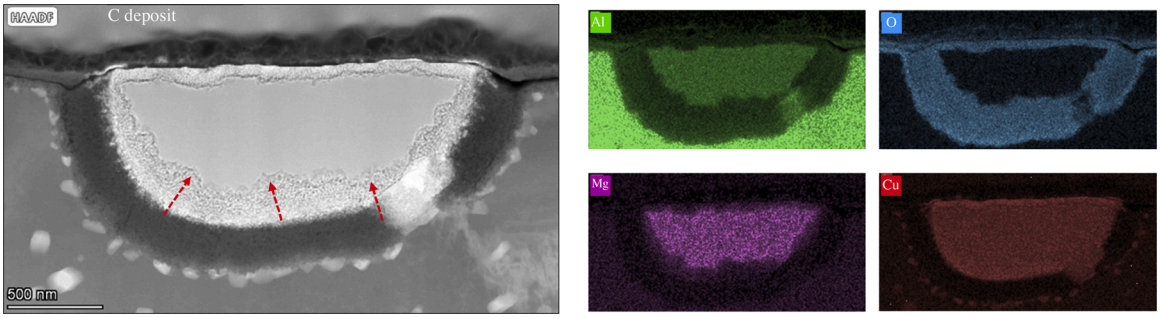

Fig. 11. STEM/EDS characterisation of S-phase. Cross-sectional STEM/EDS analysis of an Al_2CuMg particle exposed to 0.01 M NaCl + 0.01 M Li_2CO_3 solution for 7 h (electrolyte thickness of approx. 2 mm), revealing the selective dissolution of Al and Mg from the particle. The lamella was fabricated with the lift-out FIB procedure.

corresponding to Li-Al LDH appear as a shoulder in the XRD spectra. This is the case for both samples exposed to 0.01 M NaCl + 0.01 M Li_2CO_3 for 2 and 7 h. Thus, a pure aluminium exposed to the studied solution for 7 h was analysed with XRD to fortify and confirm the above hypothesis of Li-Al LDH formation. As can be seen, the pure aluminium sample shows a solo strong reflection related to the basal (003) plane. Thus, the formation of Li-Al LDH takes place as a direct consequence of the lithium-based conversion process according to the XRD results. Morphological investigations revealed that this can happen through the appearance of a columnar morphology after a 2800-s exposure at the latest.

3.5. Exposure to a sodium carbonate solution (lithium-free)

Our recent work on the cross-sectional chemical composition of the conversion layer has shown a relatively homogeneous distribution of lithium throughout the different sub-layers [17]. In order to better understand how its presence affects the layer formation, we have exposed AA2024-T3 samples to a lithium-free 0.01 M NaCl + 0.01 M Na_2CO_3 solution (pH 10.6) and in an identical condition in terms of the electrolyte thickness (approx. 4 mm). The results related to the electrochemical and morphological analysis are shown in Fig. 13. In Fig. 13a, we see the evolution of the OCP values over 5 h of exposure during which the system acquires OCP values similar to those for the lithium-containing system. As can be seen, the system shows nearly identical behaviour and values during the first 1500s (Compare the inset here and Fig. 1). Afterwards, the OCP reaches a state of little change at −1200 mV until 3 h. However, the system experiences an abrupt rise in the OCPs values, reaching −400 mV in the next 2 h of exposure. Given the morphological evolutions of the alloy matrix and the different IMPs presented in Fig. 13b–e, we notice a clear dissimilarity of the morphology in the absence and presence of lithium. As is evident, the alloy matrix has severely been corroded, revealing a typical corrosion-attack morphology observed for aluminium in alkaline environments [34,35]. A thin but highly porous layer of aluminium hydroxide is merely formed. S-phase particles are found in a dealloyed and trenched condition where no conversion layer has been formed. Besides, the alloy matrix has not been trenched around Al_2Cu and constituent phase particles; however, it has uniformly but deeply been dissolved during the exposure. It seems that lithium plays a crucial role in the stabilisation of the corrosion products in the studied alkaline environment, causing the conversion process to occur.

In the absence of lithium, the pre-existing surface aluminium oxide is just dissolved during the first 60 s, resulting in a decrease in the OCP value [32]. Subsequently, the massive dissolution of the alloy matrix comes about and this leads to a higher concentration of $Al(OH)_4^-$ at the

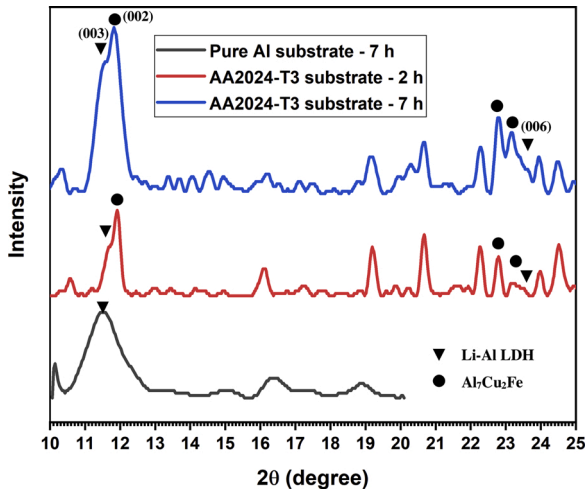

Fig. 12. XRD patterns of the conversion layer formed on AA2024-T3 and pure aluminium after exposure to 0.01 M NaCl + 0.01 M Li_2CO_3. The (003) and (006) peaks are characteristic for Li-Al LDH. The AA2024-T3 sample shows other reflections originating from different intermetallic compounds; some of the peaks corresponding to Al_7Cu_2Fe show up at the grazing angles very close to the characteristic Li-Al LDH peaks.

surface. This phenomenon causes an impact on the kinetics of aluminium dissolution with time (i.e., higher anodic Tafel slope), emerging as an increase in the OCP value [34]. The mass transfer of Al $(OH)_4^-$ ions from the surface to the bulk solution reaches a steady state condition after 500 s; that is why we see a plateau in the OCP plot from 500 s to 3 h. Since, $Al(OH)_4^-$ is the only soluble species in the studied alkaline environment [36], the porous aluminium hydroxide (acting as the intermediate [32,37]) layer becomes stable upon the supersaturation of the limited solution (i.e., 1.23 mL solution for 3.14 cm^2 area of the sample). This is associated with the abrupt increase in the OCP values since the formed layer can slow down the anodic dissolution of the alloy matrix. In addition, the gradual copper enrichment of the surface and S-phase particles as a direct consequence of the alloy matrix dissolution and dealloying, respectively, can contribute to the OCP increase at different stages of exposure as well. In fact, Cu-rich regions can increase cathodic activity of the surface through accommodating water and oxygen reduction reactions, leading to an increase in the OCP values. In comparison, the conversion process can take place in the presence of lithium in the vicinity of the surface where the required local supersaturation is fulfilled at Stage III. We discuss the mechanism of relevance in detail in the next section.

4. Local formation mechanism of the conversion layer

Top-view and cross-sectional FIB/SEM observations along with the recorded OCP values can elucidate how the alloy matrix and different IMPs evolve during the conversion process in the lithium carbonate-containing solution as shown schematically in Fig. 14. As discussed earlier, the supersaturation of the solution by $Al(OH)_4^-$ ions of the solution is of critical stage for the initiation of the conversion process. The supersaturation is fulfilled through the direct dissolution of the substrate. If the solution can acquire the required supersaturation locally, the conversion layer can take place consequently at those locations. This

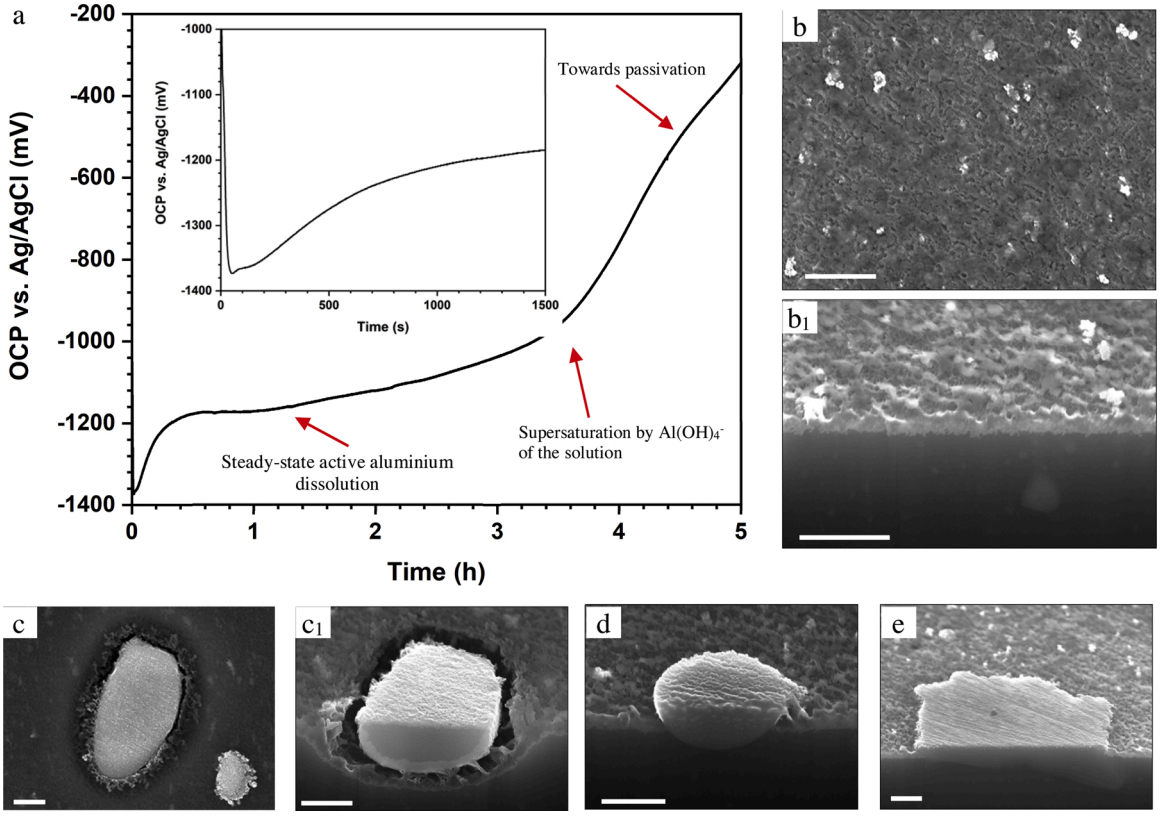

Fig. 13. Electrochemical and morphological evaluations of AA2024-T3 exposed to 0.01 M NaCl + 0.01 M Na_2CO_3 (lithium-free solution; pH 10.6) for 5 h. (a) OCP response of AA2024-T3 over time. The inset shows a closer look at the OCP behaviour at early stages of exposure. (b and b_1) Top-view and cross-sectional SEM images of the alloy matrix, revealing the surface to be severely corroded while a highly porous thin aluminium hydroxide layer has been formed during the exposure. (c and c_1) Top-view and cross-sectional SEM images of an Al_2CuMg particle, showing that the particle has undergone dealloying and besides the surrounding alloy matrix has been fully trenched. Cross-sectional SEM image of (d) an Al_2Cu and (e) a constituent-phase particle which have been surface-dealloyed while their adjacent matrix has been dissolved significantly (stage tilt 52°). The scale bar is 1 μm.

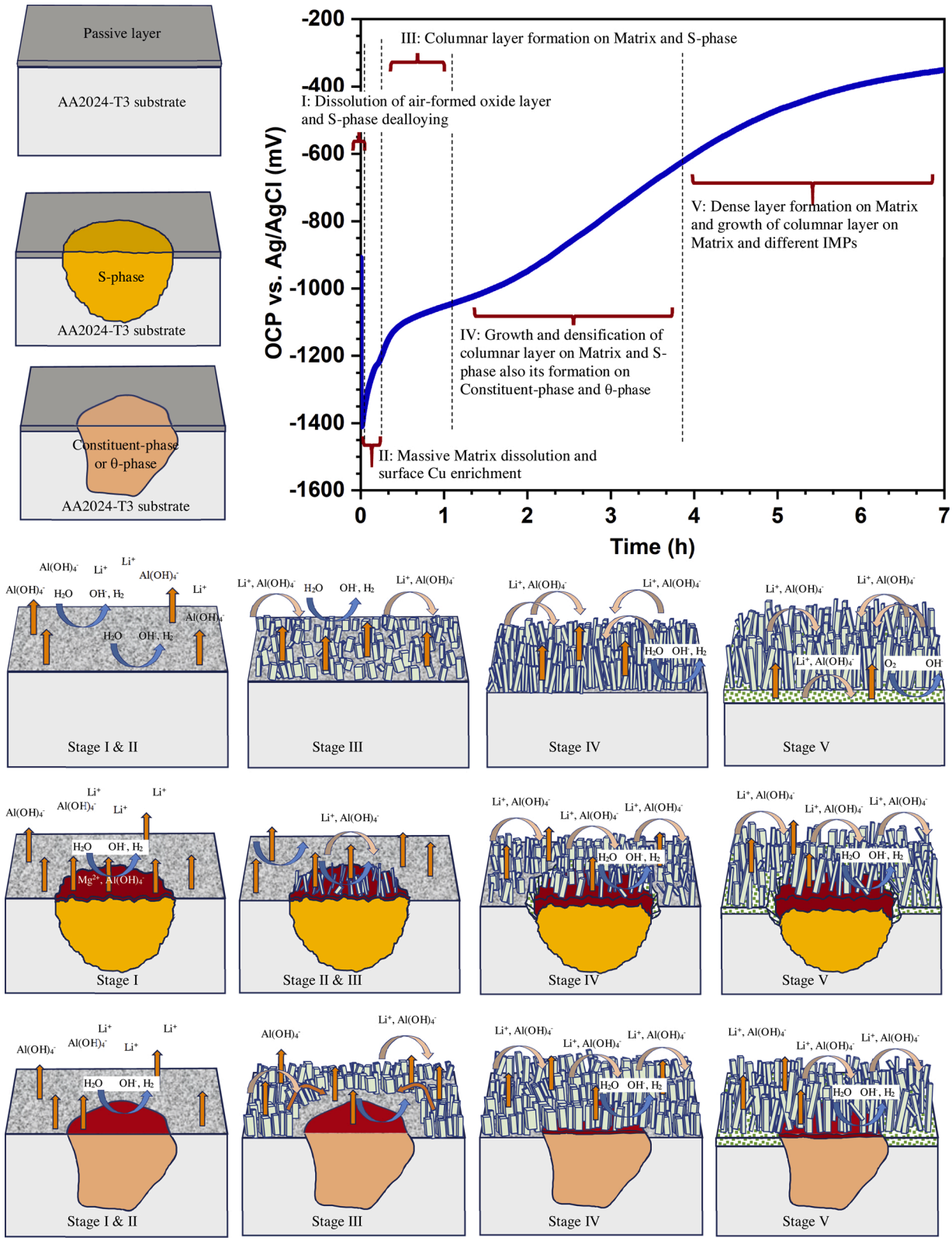

Fig. 14. The formation mechanism of the conversion layer on AA2024-T3. 3D schematic view of formation mechanism of the conversion layer on different regions in the alloy linked to the OCP response of the whole system. The probable corrosion and precipitation reactions taking place on the alloy matrix and also around IMPs are depicted in detail. The columnar morphology is the initial layer being formed over the matrix and it is the only layer formed over IMPs. The dense layer is established with a proceeding dissolution front into the alloy matrix or within trenches around S-phase particles. Copper-rich regions like the top-surface parts of the dealloyed IMPs or nanoscopic remnants are responsible for supporting cathodic reactions.

phenomenon is well pronounced for S-phase particles where a fast dealloying can effectively enhance the local supersaturation and hence the local lithium-based conversion process.

4.1. Alloy matrix

At Stage I, the alloy matrix initially loses its passivity in the studied alkaline environment, inducing a drop in the OCP value during the first 60 s. At Stage II, the process proceeds by active dissolution of the alloy matrix; the kinetics of aluminium dissolution decreases gradually due to the accumulation of $Al(OH)_4^-$ ions, which form through the transformation of Al^{3+} to $Al(OH)_3$ and then to $Al(OH)_4^-$ under the alkaline conditions present at the surface. In addition, the surface gradually becomes enriched in copper as the alloy matrix holds 0.2−0.5 at% Cu and besides due to dealloying of the nanoscopic IMPs (i.e. S-phase and dispersoids) [38]. As discussed in Section 3.5, these two phenomena bring about a gradual increase in the OCP value. In contrast to the lithium-free solution, the conversion layer nucleates and starts growing in a columnar morphology upon reaching the required supersaturation at the surface (Stage III). At Stage (IV), the dissolution front still penetrates into the alloy matrix and consequently the columns further grow and get entangled with time. The OCP continues to increase in this period as the alloy matrix progressively acquires passivity (i.e., anodic Tafel slope increases). Although the columnar layer is not highly protective, the entangled network of the long columns can effectively slow down the dissolution rate. This causes a positive impact on the densification of the conversion layer; thus, the next sublayer which appears is a dense layer close to the substrate (Stage V). Simultaneously, the columnar layer grows through direct precipitation of the Li-containing products (e.g., Li-Al LDH) from the saturated solution, resulting in coarsening of the columnar morphology. At Stage V, the system experiences a nearly stabilised condition and the OCP curve plateaus due to the passivation by the lithium-based conversion layer.

4.2. S-phase (Al_2CuMg) particles

Al_2CuMg compound is a highly electrochemically active phase that quickly interacts with the alkaline Li-containing solution upon exposure (Stage I). At Stage II, S-phase particles release $Al(OH)^{4-}$ and Mg^{2+} in the studied solution as a direct consequence of dealloying causing the local supersaturation of the solution and copper enrichment of the corroding particles. The former triggers the formation of the columnar morphology over S-phase particles preceding that on the alloy matrix. The latter gives rise to the increase in the OCP values by increasing cathodic activities of the surface. At Stage III, the columnar layer grows and this is associated with further penetration of dealloying. Stage IV comes with further growth of the columnar layer on the particle and adjacent at the alloy matrix, although the preferential trenching of the alloy matrix takes place too. There is no difference between Stage IV and V for the S-phase particle where the further columnar layer growth, particle dealloying and alloy matrix trenching simultaneously but sluggishly occur.

4.3. Al_2Cu and constituent phase particles

Al_2Cu and constituent phase particles show a high electrochemical stability in the alkaline lithium-containing solution, undergoing a slight dealloying throughout the 7-h exposure. At Stage I and II, they insignificantly release $Al(OH)_4^-$ into the solution due to sluggish dealloying disabling to reach supersaturation. Thus, the alloy matrix is the only source for providing $Al(OH)_4^-$ ions as the main component of the lithium-based conversion layer. That is why the conversion layer is observed over the whole alloy matrix except the region surrounding the Al_2Cu and constituent phase particles (Stage III). Similar to S-phase particles, the only columnar layer grows through the precipitation during Stage IV and V while the alloy matrix acquires a dense-like sublayer at Stage V by further penetrating into the depth.

5. Conclusions

While our previous works provided a general lithium-based conversion layer formation mechanism, here we unravelled the laterally resolved formation mechanisms of the layer at the matrix and IMPs of AA2024-T3 in a condition mimicking coating defects when lithium carbonate is used as the leaching inhibitor. With sub-micron resolved top-view and cross-sectional FIB/SEM analysis along with OCP recording, we distinguished 5 stages (out of a 7-h exposure) during the conversion process in which the alloy matrix and different IMPs evolve morphologically, compositionally and electrochemically. We found that AA2024-T3 does not acquire passivation in early exposure times up to 800 s (Stage I and II). Passivity loss leads to the initial OCP drop during the first 60 s. However, active alloy matrix dissolution and surface Cu-enrichment mainly contribute to the rise in OCP values by modifying anodic and cathodic activities, respectively. Upon reaching local supersaturation at Stage III, the conversion layer appears in a columnar morphology on S-phase, alloy matrix and other intermetallic compounds in a chronological order. This is associated with a rise in OCP values due to the diminished kinetics of the anodic aluminium dissolution. Faster dealloying of S-phase can enhance the conversion process by providing relatively rapidly $Al(OH)_4^-$ ions (local supersaturation). Besides, lithium plays a critical role in stabilising the corrosion products; no conversion process occurs under the same exposure conditions but in the absence of lithium. At Stage IV (starting from approx. 1 h and lasting until 4 h), the columnar layer grows and the OCP values rise. Finally, Stage V is involved with the formation of the dense-like layer closest to the alloy matrix while IMPs are merely covered with a columnar layer. At this stage, the system acquires passivation, revealing a plateaued OCP curve owing to the electrochemical stabilisation (i.e., nearly constant anodic and cathodic behaviour). Finally, the critical role of lithium in the conversion process was revealed through complementary experiments in a sodium carbonate solution and X-ray diffraction analysis.

CRediT authorship contribution statement

A. Kosari: Conceptualization, Methodology, Validation, Investigation, Writing - original draft. **F. Tichelaar:** Investigation, Writing - review & editing. **P. Visser:** Conceptualization, Writing - review & editing. **H. Zandbergen:** Writing - review & editing, Supervision. **H. Terryn:** Conceptualization, Writing - review & editing, Supervision. **J.M.C. Mol:** Conceptualization, Writing - review & editing, Supervision.

Declaration of Competing Interest

With no conflict of interest, we declare that the research material is original and has neither been published previously nor been submitted for publication elsewhere.

Acknowledgments

This work is part of the research program Understanding Processes using Operando Nanoscopy (UPON) with project number 14205 (B2), which is financed by the Dutch Research Council (NWO) and partially by AkzoNobel. Mr. Ruud Hendrikx at the Materials Science and Engineering Department, TU Delft is acknowledged for the XRD measurements.

Appendix A. Supplementary data

Supplementary material related to this article can be found, in the online version, at doi:https://doi.org/10.1016/j.corsci.2021.109651.

References

[1] P. Visser, H. Terryn, J.M.C. Mol, Active corrosion protection of various aluminium alloys by lithium-leaching coatings, Surf. Interface Anal. 51 (2019) 1276–1287.

[2] P. Visser, Y. Liu, H. Terryn, J.M.C. Mol, Lithium salts as leachable corrosion inhibitors and potential replacement for hexavalent chromium in organic coatings for the protection of aluminum alloys, J. Coat. Technol. Res. 13 (2016) 557–566.
[3] O. Gharbi, S. Thomas, C. Smith, N. Birbilis, Chromate replacement: what does the future hold? NPJ Mater. Degrad. 2 (2018) 1–8.
[4] D. Mata, M. Serdechnova, M. Mohedano, C.L. Mendis, S.V. Lamaka, J. Tedim, T. Hack, S. Nixon, M.L. Zheludkevich, Hierarchically organized Li–Al-LDH nanoflakes: a low-temperature approach to seal porous anodic oxide on aluminum alloys, RSC Adv. 7 (2017) 35357–35367.
[5] C.D. Dieleman, P.J. Denissen, S.J. Garcia, Long-term active corrosion protection of damaged Coated-AA2024-T3 by embedded electrospun inhibiting nanonetworks, Adv. Mater. Interfaces 5 (2018), 1800176.
[6] J. Gui, T.M. Devine, Influence of lithium on the corrosion of aluminum, Scr. Metall.;(United States) 21 (1987).
[7] R.G. Buchheit, M.D. Bode, G.E. Stoner, Corrosion-resistant, chromate-free talc coatings for aluminum, Corrosion 50 (1994) 205–214.
[8] C.A. Drewien, M.O. Eatough, D.R. Tallant, C.R. Hills, R.G. Buchheit, Lithium-aluminum-carbonate-hydroxide hydrate coatings on aluminum alloys: composition, structure, and processing bath chemistry, J. Mater. Res. 11 (1996) 1507–1513.
[9] P. Visser, S. Hayes, in: WIP Organization (Ed.), Anti-Corrosive Coating Composition, WO, 2010, p. A1, 112605.
[10] P. Visser, Y. Liu, X. Zhou, T. Hashimoto, G.E. Thompson, S.B. Lyon, L.G. van der Ven, A. Mol, H.A. Terryn, The corrosion protection of AA2024-T3 aluminium alloy by leaching of lithium-containing salts from organic coatings, Faraday Discuss. 180 (2015) 511–526.
[11] Y. Liu, P. Visser, X. Zhou, S.B. Lyon, T. Hashimoto, A. Gholinia, G.E. Thompson, G. Smyth, S.R. Gibbon, D. Graham, An investigation of the corrosion inhibitive layers generated from lithium oxalate-containing organic coating on AA2024-T3 aluminium alloy, Surf. Interface Anal. 48 (2016) 798–803.
[12] P. Visser, K. Marcoen, G.F. Trindade, M. Abel, J. Watts, T. Hauffman, J.M.C. Mol, H. Terryn, The chemical throwing power of lithium-based inhibitors from organic coatings on AA2024-T3, Corros. Sci. 150 (2019) 194–206.
[13] P. Visser, A. Lutz, J.M.C. Mol, H. Terryn, Study of the formation of a protective layer in a defect from lithium-leaching organic coatings, Prog. Org. Coat. 99 (2016) 80–90.
[14] P. Visser, H. Terryn, J.M.C. Mol, On the importance of irreversibility of corrosion inhibitors for active coating protection of AA2024-T3, Corros. Sci. 140 (2018) 272–285.
[15] K. Marcoen, P. Visser, G.F. Trindade, M.-L. Abel, J.F. Watts, J.M.C. Mol, H. Terryn, T. Hauffman, Compositional study of a corrosion protective layer formed by leachable lithium salts in a coating defect on AA2024-T3 aluminium alloys, Prog. Org. Coat. 119 (2018) 65–75.
[16] Y. Liu, P. Visser, X. Zhou, S.B. Lyon, T. Hashimoto, M. Curioni, A. Gholinia, G. E. Thompson, G. Smyth, S.R. Gibbon, Protective film formation on AA2024-T3 aluminum alloy by leaching of lithium carbonate from an organic coating, J. Electrochem. Soc. 163 (2015) C45.
[17] A. Kosari, P. Visser, F. Tichelaar, S. Eswara, J.N. Audinot, T. Wirtz, H. Zandbergen, H. Terryn, J.M.C. Mol, Cross-sectional characterization of the conversion layer formed on AA2024-T3 by a lithium-leaching coating, Appl. Surf. Sci. 512 (2020), 145665.
[18] P. Visser, M. Meeusen, Y. Gonzalez-Garcia, H. Terryn, J.M.C. Mol, Electrochemical evaluation of corrosion inhibiting layers formed in a defect from lithium-leaching organic coatings, J. Electrochem. Soc. 164 (2017) C396.
[19] P. Visser, Y. Gonzalez-Garcia, J.M.C. Mol, H. Terryn, Mechanism of passive layer formation on AA2024-T3 from alkaline lithium carbonate solutions in the presence of sodium chloride, J. Electrochem. Soc. 165 (2018) C60.
[20] A.E. Hughes, N. Birbilis, J.M.C. Mol, S.J. Garcia, X. Zhou, G.E. Thompson, High strength Al-alloys: microstructure, corrosion and principles of protection, in: A. Zaki (Ed.), Recent Trends in Processing and Degradation of Aluminium Alloys, 2011.
[21] A. Boag, R.J. Taylor, T.H. Muster, N. Goodman, D. McCulloch, C. Ryan, B. Rout, D. Jamieson, A.E. Hughes, Stable pit formation on AA2024-T3 in a NaCl environment, Corros. Sci. 52 (2010) 90–103.
[22] Y. Zhu, K. Sun, G.S. Frankel, Intermetallic phases in aluminum alloys and their roles in localized corrosion, J. Electrochem. Soc. 165 (2018) C807.
[23] G.O. Ilevbare, O. Schneider, R.G. Kelly, J.R. Scully, In situ confocal laser scanning microscopy of AA 2024-T3 corrosion metrology: I. Localized corrosion of particles, J. Electrochem. Soc. 151 (2004) B453.
[24] N. Birbilis, R.G. Buchheit, Electrochemical characteristics of intermetallic phases in aluminum alloys: an experimental survey and discussion, J. Electrochem. Soc. 152 (2005) B140.
[25] A. Kosari, H. Zandbergen, F. Tichelaar, P. Visser, P. Taheri, H. Terryn, J.M.C. Mol, In-situ nanoscopic observations of dealloying-driven local corrosion from surface initiation to in-depth propagation, Corros. Sci. 177 (2020), 108912.
[26] A. Kosari, F. Tichelaar, P. Visser, H. Zandbergen, H. Terryn, J.M.C. Mol, Dealloying-driven local corrosion by intermetallic constituent particles and dispersoids in aerospace aluminium alloys, Corros. Sci. 177 (2020), 108947.
[27] A.E. Hughes, R. Parvizi, M. Forsyth, Microstructure and corrosion of AA2024, Corros. Rev. 33 (2015) 1–30.
[28] R.G. Buchheit, R.P. Grant, P.F. Hlava, B. McKenzie, G.L. Zender, Local dissolution phenomena associated with S phase (Al2CuMg) particles in aluminum alloy 2024-T3, J. Electrochem. Soc. 144 (1997) 2621.
[29] J. Mayer, L.A. Giannuzzi, T. Kamino, J. Michael, TEM sample preparation and FIB-induced damage, MRS Bull. 32 (2007) 400–407.
[30] E. McCafferty, Kinetics of Corrosion, Springer, 2010.
[31] N. Birbilis, Y.M. Zhu, S.K. Kairy, M.A. Glenn, J.-F. Nie, A.J. Morton, Y. Gonzalez-Garcia, H. Terryn, J.M.C. Mol, A.E. Hughes, A closer look at constituent induced localised corrosion in Al-Cu-Mg alloys, Corros. Sci. 113 (2016) 160–171.
[32] G.T. Burstein, R.J. Cinderey, Evolution of the corrosion potential of repassivating aluminium surfaces, Corros. Sci. 33 (1992) 475–492.
[33] Y. Waseda, E. Matsubara, K. Shinoda, X-Ray Diffraction Crystallography: Introduction, Examples and Solved Problems, Springer Science & Business Media, 2011.
[34] K.C. Emregül, A.A. Aksüt, The behavior of aluminum in alkaline media, Corros. Sci. 42 (2000) 2051–2067.
[35] S.-I. Pyun, S.-M. Moon, Corrosion mechanism of pure aluminium in aqueous alkaline solution, J. Solid State Electrochem. 4 (2000) 267–272.
[36] M. Pourbaix, Atlas of electrochemical equilibria in aqueous solution, NACE 307 (1974).
[37] M.R. Tabrizi, S.B. Lyon, G.E. Thompson, J.M. Ferguson, The long-term corrosion of aluminium in alkaline media, Corros. Sci. 32 (1991) 733–742.
[38] N. Wint, Z.S. Barrett, G. Williams, H.N. McMurray, The study of AA2024 de-alloying using luminol electrogenerated chemiluminescence imaging, J. Electrochem. Soc. 166 (2019) C3417.